



A method for improving the performance of the 2σ lightning jump algorithm for nowcasting hail

Ye Tian^a, Wen Yao^{b,*}, Yue Sun^c, Yu Wang^{d,e}, Xulin Liu^a, Tao Jiang^a, Longbin Zhang^a, Lei Meng^a, Lu Wang^a, Xueqi Sun^a, Hailong Wang^a

^a Beijing Meteorological Observation Center, Beijing Meteorological Service, Beijing 100089, China

^b State Key Laboratory of Severe Weather, Chinese Academy of Meteorological Sciences, Beijing 100081, China

^c Key Laboratory of Cloud-Precipitation and Severe Storms, Center of Disaster Reduction, Institute of Atmospheric Physics, Chinese Academy of Sciences, Beijing 100029, China

^d Wuhan NARI Limited Liability Company, State Grid Electric Power Research Institute, Wuhan 430074, China

^e Hubei Province Key laboratory of Lightning Risk Prevention for Power Grids, Wuhan 430074, China

ARTICLE INFO

Keywords:

Hail nowcasting
Lightning jump
Dual-polarization radar
Hydrometeor classification

ABSTRACT

Studies have shown that the 2σ lightning jump (LJ) algorithm exhibits good performance for severe weather warnings but continues to produce a high false alarm rate (FAR). A method is proposed in this study for improving the 2σ LJ hail warning performance by combining the hydrometeor classification results of dual-polarization radar with the 2σ LJ algorithm. A total of 17 hail events occurred across Jiangsu, China on April 29th -30th, 2021. Dual-polarization radar and hail observation data were used to calculate five variables, including the rate, first derivative (FD), rate of rate (rate2), second derivative (SD) and the rate of FD (FD_rate), for large hail (HA), graupel and small hail (G/SH), rain and hail (RH), and ice crystal (IC) grid point numbers. The evolution of these variables was compared and analyzed. The results indicate that the positive local peaks of rate2 of the HA and G/SH grid point numbers can be used to effectively identify valid and invalid LJs. Removing the identified invalid LJs reduces the FAR without affecting the probability of detection (POD), thus improving the hail warning performance of the 2σ LJ algorithm. This method was tested for the aforementioned 17 hail events. The rejection rate of invalid LJs reached 69.6%, and the false identification rate of valid LJs was only 9/29 (31%). The proposed method for hail warning had a POD equal to that of the conventional 2σ LJ algorithm (100%) and a significantly lower FAR (29.2% versus 58.5%). Moreover, the critical success index (CSI) of the proposed method (70.8%) was considerably higher than that (41.5%) of the conventional 2σ LJ algorithm. However, the average early warning lead time of the proposed method (35.1 min) was slightly lower than that (37.9 min) of the conventional 2σ LJ algorithm. The proposed method is superior to the conventional 2σ LJ algorithm in terms of the FAR and CSI for hail warning and therefore considerably improves the ability of the 2σ LJ algorithm to produce refined early warnings of hail or even severe weather for meteorological services.

1. Introduction

Hail is a common meteorological natural disaster. Hail, thunderstorms, gales, tornadoes, and flash floods have increasingly been causing casualties and property losses (Prein and Holland, 2018). In North America alone, the annual loss due to hail exceeds US \$10 billion (Allen et al., 2020). China also suffers frequent hail damage. For example, the annual economic loss in China due to hail reached hundreds of millions to several billion yuan in the 1990s (Ma, 1994), and the economic loss in Jiangsu Province alone was as high as 1.37 billion yuan from 2000 to

2003 (Bao et al., 2012). Therefore, effective hail warning is highly desirable. However, due to the sudden and localized nature of hail, the early warning and forecasting of hail has always been difficult.

At present, scholars use various means to achieve early warning of severe convective weather that may produce hail, such as Doppler radar monitoring, high-resolution satellite and satellite-borne sensor monitoring, diagnosis of circulation features and physical quantity characteristics, cloud microphysics, numerical weather model simulation, and machine learning methods (Ni et al., 2017; Shi et al., 2019; Bang and Cecil, 2019; Bruick et al., 2019; Murillo and Homeyer, 2019; Laviola

* Corresponding author.

E-mail address: yaowen@cma.gov.cn (W. Yao).

<https://doi.org/10.1016/j.atmosres.2022.106404>

Received 22 March 2022; Received in revised form 8 July 2022; Accepted 19 August 2022

Available online 22 August 2022

0169-8095/© 2022 Elsevier B.V. All rights reserved.

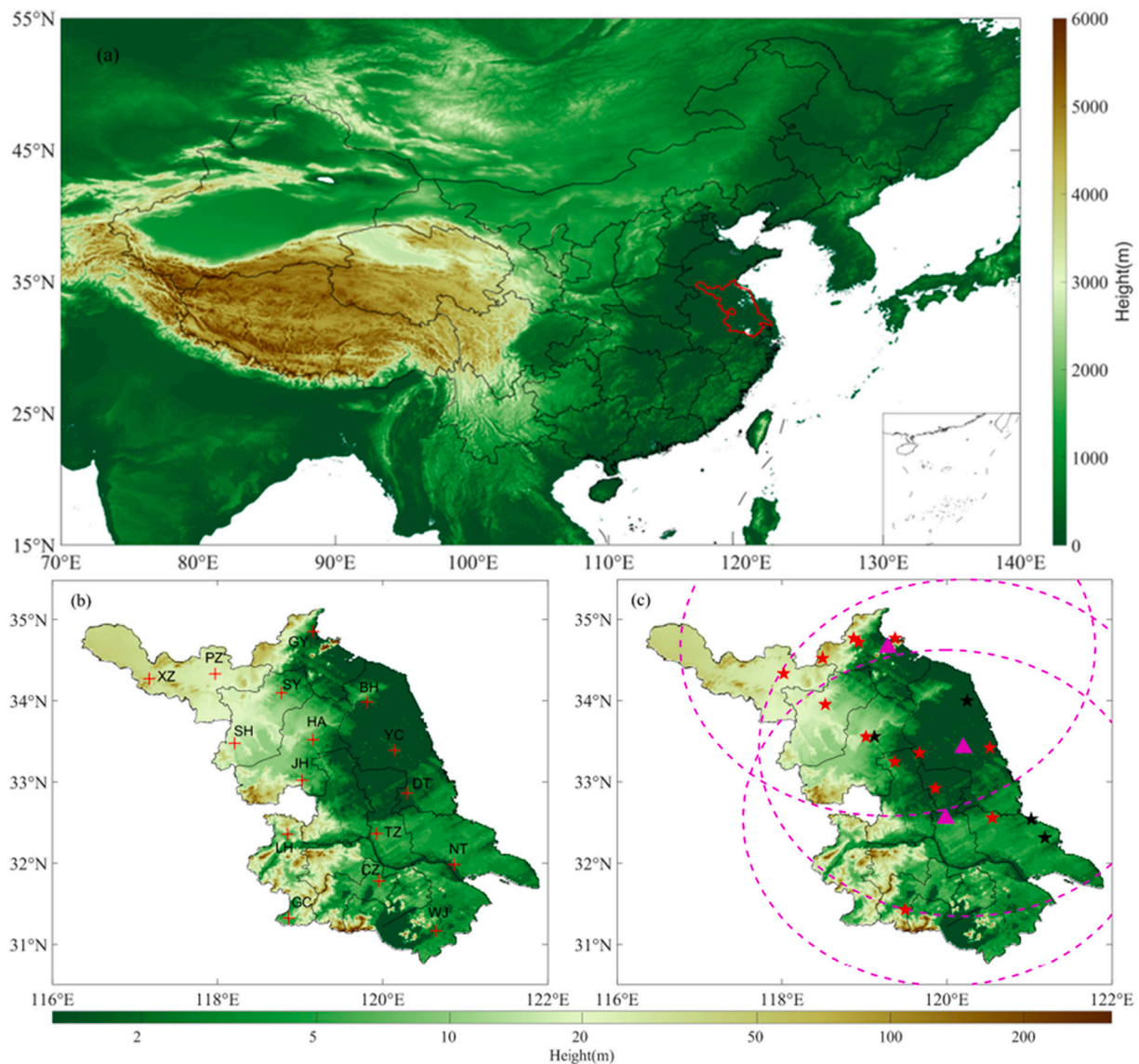


Fig. 1. (a) An elevation map of China, where the red polygon shows the location of Jiangsu Province, (b) a distribution map of the lightning positioning system of the Electric Power System of Jiangsu Province, in which the red crosses represent the substations of the lightning positioning system, and (c) a schematic diagram showing the radar and hail locations investigated in this study, in which the magenta triangles represent the radar stations, the black stars represent the hail events that occurred on April 29, the red stars represent the hail events that occurred on April 30, and the magenta dotted circles indicate the detection range of each radar. (For interpretation of the references to colour in this figure legend, the reader is referred to the web version of this article.)

et al., 2020; Kumjian and Lombardo, 2020; Burke et al., 2020; Gensini et al., 2021). Many studies have found that the flash rate (FR) rapidly increases before the occurrence of severe weather (Chronis et al., 2015; Wapler, 2017; Curtis et al., 2018; Wu et al., 2018; Farnell and Rigo, 2020a; Murphy and Said, 2020); this is called a lightning jump (LJ) (Williams et al., 1999).

Many scholars have achieved good results in early warning of severe weather (including hail), such as high probability of detection (POD), by using lightning data-based LJ algorithms. However, LJ algorithms also produce a considerable number of false warnings for severe weather, that is, a high false alarm rate (FAR). Gatlin (2007) obtained a FAR of 41.9% for tornado warnings using an LJ algorithm. Schultz et al. (2009) studied 85 thunderstorms in the Washington and Tennessee basins of the United States and compared and analyzed the hail, gale and tornado warning performances of six different LJ algorithms, in which the FAR of the 2σ LJ algorithm was 33%. Gatlin and Goodman (2010) analyzed the hail and tornado warning performance of their own LJ algorithm on 20 thunderstorms; although the POD was 90%, the FAR reached 37%.

Schultz et al. (2011) further studied the warning performance of the 2σ LJ algorithm on 711 thunderstorms and found that the FAR for early warning reached 36% and 53% using total lightning flash data and cloud-to-ground (CG) flash data alone, respectively. The severe weather criteria in the previous three studies were hail diameter ≥ 19 mm and wind speed ≥ 26 m/s. Miller et al. (2015) identified single-cell thunderstorms in the summers of 2012 and 2013 in the central Appalachian Mountains of the United States by clustering the lightning data of the Earth Networks Total Lightning Network. They obtained an FAR exceeding 85% for early warning of severe weather (including hail) from these single-cell thunderstorms using the 2σ LJ algorithm. Similarly, Murphy (2017) analyzed 3350 thunderstorms in 2015 and 2016 based on the detection results of intracloud flashes and CG flashes of the National Lightning Detection Network (NLDN) and obtained an FAR of 85% for early warning of severe weather (including hail) using the 2σ LJ algorithm. Farnell et al. (2017) used total lightning flash data to conduct early warning studies on 48 cases of hail and gusts without using radar data and achieved excellent performance (POD = 75% and FAR = 10%).

Farnell and Rigo (2020b) analyzed heavy precipitation events in Catalonia from 2013 to 2018 and obtained an FAR of 10% for early warning using LJs. The severe weather criteria in these two studies were hail diameter ≥ 20 mm and wind speed ≥ 25 m/s. The lightning data included both CG and intracloud flashes detected by low and very high frequency sensors, respectively. Tian et al. (2019) studied 148 cases of hail (hail diameter ≥ 5 mm) in the Beijing area from 2015 to 2017 and obtained a POD of 81.8% and an FAR of 38.6% for hail warning using the 2σ LJ algorithm. Nisi et al. (2020) used ground-based lightning location network data and $>30,000$ hailstorms in the Alps region (2012–2017) to study various lightning parameters (FR, flash density, peak current, and LJ). They found that the POD for LJ-based hail warning was only 45%, while the FAR reached 30%. In summary, the FAR of the 2σ LJ algorithm exceeded 30% in most studies and exceeded 80% in some studies. The high FAR considerably reduces the universality of the 2σ LJ algorithm for application to meteorological services. Therefore, a new method should be developed to reduce the FAR of the 2σ LJ algorithm in early warning without reducing the POD.

In recent years, the S-band Doppler radars used by the China Meteorological Administration have gradually been upgraded to dual-polarization radars. Dual-polarization radar can obtain observations in both the horizontal and vertical polarization channels. The observed polarimetric variables can respond to the characteristics of hydrometeor particles, such as size, shape, orientation and uniformity, providing a physical basis for hydrometeor classification (HC). In the past over 20 years, HC methods based on fuzzy logic algorithms have been improved and used in operation (Vivekanandan et al., 1999; Straka et al., 2000; Liu and Chandrasekar, 2000; Zrníc et al., 2001; Park et al., 2009; Dolan and Rutledge, 2009; Snyder et al., 2010; Zhang et al., 2019). These methods can provide classifications such as rain, ice crystal, snow, graupel and hail in radar detection space, monitoring hail and freezing hazards. Hail size discrimination studies based on HC have also been conducted in recent years (Ryzhkov et al., 2013a, 2013b; Ortega et al., 2016).

In terms of thunderstorm monitoring by dual-polarization radar, the change in observed polarimetric variables and retrieved orientation of ice crystals before and after lightning were the focus of early studies (Caylor and Chandrasekar, 1996; Zrníc and Ryzhkov, 1999; Scott et al., 2001). In recent years, some studies have applied the HC method and pointed out the close relationship between lightning and graupel particles in clouds (Lund et al., 2009; Carey et al., 2014, 2019; Mecikalski et al., 2015).

Z_{DR} and K_{DP} column information from dual-polarization radar can be used to analyze the relationship between updrafts and the characteristics of lightning activity during the mixing stage of a supercell (Sharma et al., 2021). Kalina et al. (2016) used S-band dual-polarization radar and total lightning flash data to statistically analyze the characteristics of the radar polarization parameters of thunderstorm clouds that caused hail accumulations of 15 to 60 cm on the ground. Kalina et al. proposed that total FR data could be used to help forecasters identify such hailstorms.

However, as the HC method can only identify hail that is already in clouds, the corresponding warning time for hail hazards could be insufficient, and a false alarm may be issued if the hail melts before reaching the ground. Therefore, it is still necessary to combine other data and methods to improve the reliability and timeliness of hail warning. Hence, we attempt to develop a method that combines the HC results of dual-polarization radar and the 2σ LJ algorithm to reduce the FAR for the early warning, thus improving the refined early warning capabilities of meteorological services for hail events.

The radar, lightning, hail and sounding data used in this study and a quality control analysis of the data are presented in the second section of this paper. In Section 3, the methods used to analyze the data are introduced, where the HC method is presented in Section 3.2 and a method for removing false alarms is presented in Section 3.3. In Section 4, two multicell thunderstorms are selected for detailed analysis, and the

Table 1
Hail events on April 29, 2021.

	Event location	Event duration (Beijing time)	Maximum hail diameter
Case 1	Linhai Town, Sheyang County, Yancheng City	18:15–18:25	5 mm
Case 2	Huaiyin District, Huaian City	18:16-unrecorded	5 mm
Case 3	Pincha Town and Yangkou Town, Nantong City	20:30–20:33	5 mm
Case 4	Juegang Street, Rudong County, Nantong City	22:00–22:03	5 mm

Table 2
Hail events on April 30, 2021.

	Event location	Event duration (Beijing time)	Maximum hail diameter
Case 1	Shilianghe Town, Donghai County, Lianyungang City	13:23–13:31	5 mm
Case 2	Huangchuan Town, Donghai District, Lianyungang City	13:34–13:40	5 mm
Case 3	Lianyung District Meteorological Bureau, Lianyungang City	14:00–14:09	5 mm
Case 4	Pizhou East Railway Station, Xuzhou City	17:00-unrecorded	10 mm
Case 5	Taolin Town, Donghai County, Lianyungang City	17:15–17:36	10 mm
Case 6	Guanmiao Town, Suyu District, Suqian City	17:00-unrecorded	10 mm
Case 7	Huai'an Meteorological Observation Station	18:14-unrecorded	50 mm
Case 8	Hengji Town, Jianhu County, Yancheng City	18:30–18:40	35 mm
Case 9	Baoying District, Yangzhou City	18:46–18:56	15 mm
Case 10	Yangmanhe Town, Haian County, Nantong City	18:50-unrecorded	10 mm
Case 11	Sanlong Town, Dafeng District, Yancheng City	19:26-unrecorded	9 mm
Case 12	Xinghua District, Taizhou City	19:37-unrecorded	10 mm
Case 13	Liyang District, Changzhou City	22:34-unrecorded	10 mm

conditions of all 17 hail events are tested and compared. The last section draws conclusions and discusses prospects.

2. Data and quality control

2.1. Hail event data

On April 29 and 30, 2021, an extreme weather event occurred in Jiangsu Province, China (Fig. 1(a)). A total of 17 hail events occurred across Jiangsu over two days. The maximum hail diameter was 50 mm. Thunderstorms and gales occurred in many regions, and the maximum wind speed reached 47.9 m/s. This severe convective weather event caused 11 deaths, 66 injuries, and serious property losses. Table 1 shows the four hail events on April 29, 2021. The maximum hail diameter on this day was 5 mm.

Table 2 shows the 13 hail events on April 30, 2021. The maximum hail diameter ranged from 5 mm to 50 mm in all thunderstorms on that day.

2.2. Radar data

Four hail events on April 29, 2021 in Yancheng City, Jiangsu Province, were analyzed using the weather radar (120°12'E, 33°25'N; elevation: 28.3 m; time resolution: 343 s), assuming that the hail-producing cell developed within the radar detection range. Of the 13

hail events on April 30, 2021, the first 12 cases were all analyzed using the radar (119°17'E, 34°39'N; elevation: 594 m; a time resolution: 335 s) in Lianyungang city, Jiangsu Province, and Case 13 was analyzed using the radar (119°59'E, 32°33'N; elevation: 58.4 m; time resolution: 323 s) in Taizhou City, Jiangsu Province. Fig. 1(c) shows the locations of the radars and individual hail events.

These three radars were upgraded to dual-polarization radar from CINRAD-SA S-band weather radar in May 2019. The system characteristics and performance of this type of radar have been analyzed in previous studies (Zhao et al., 2019; Wu et al., 2022). The observed variables include horizontal reflectivity (Z_H), Doppler radial velocity (V), spectral width of Doppler velocity (W), signal-to-noise ratio (SNR), differential reflectivity (Z_{DR}), copolar correlation coefficient (ρ_{HV}), differential propagation phase (Φ_{DP}) and specific differential propagation phase shift (K_{DP}). An operational volume scan mode on nine layers is applied with an elevation range from 0.5° to 19.5°. The sampling resolution in the azimuth and elevation directions is 1°, and the radial resolution is 250 m.

2.3. Lightning data

The lightning data used in this paper came from the lightning location network of the Electric Power System of Jiangsu Province, as shown in Fig. 1(b). The lightning location network includes a total of 16 stations, with an average baseline length of 97.4 km and a single-station detection range of approximately 200 km. This networking system locates flashes using the time difference of arrival, direction finding, and direction finding combined with the time difference of arrival. The system can locate CG flashes but not intracloud flashes. This system detects CG flashes at an efficiency of 90% and a positioning error of 200–500 m (Chen et al., 2010, 2016). The range of the CG lightning data is 30°N–36°N and 116°E–123°E, which covers all of Jiangsu Province. The CG lightning data include the time, latitude and longitude, strength of the return current, type of return stroke (first return stroke or subsequent return strokes), and number of positioning stations. The first return stroke and subsequent return strokes were combined into a CG lightning flash process.

2.4. Sounding data

In this study, we used the sounding data from three stations, namely, Xuzhou, Yancheng, and Nanjing. In the actual processing, based on the principle of spatial correlation, the sounding data of the sounding station closest to the strong convective cell that produced the hail were selected. Additionally, based on the principle of time correlation, the sounding data at 08:00 were selected for the strong convective cells between 02:00 and 14:00 (Beijing time), and the sounding data at 20:00 were selected for the rest of the time. The primary sounding data include the observation results of atmospheric pressure, geopotential height, temperature, dew point, wind direction, and wind speed. In this paper, geopotential height and temperature were selected to calculate the vertical temperature profile of the station.

2.5. Quality control of radar data

Data quality control of polarimetric variables is necessary before applying HC. To reduce the effects of noise at the boundary layer and nonweather signals, the data points with ρ_{HV} values lower than 0.4 and the 10 points with moving standard deviation values >0.1 were masked. The ρ_{HV} was compensated with the SNR (Liu et al., 1994; Schuur et al., 2003). The K_{DP} was reconstructed by spline estimation (Wang and Chandrasekar, 2009) after the Φ_{DP} was refined by the iteration filtering scheme of Sun et al. (2020).

3. Method

3.1. LJ algorithm and identification method for strong convective cells

In this paper, the thunderstorm identification tracking analysis and nowcasting (TITAN) algorithm was used to identify strong convective cells (Dixon and Wiener, 1993), and the 2σ LJ algorithm developed by Schultz et al. (2011) (the FR threshold is set to 2) was used to determine LJs. A detailed description of the aforementioned algorithms can be found in Tian et al. (2019) and will not be presented here. A 2σ LJ that occurs up to 60 min before a hail event is called a valid LJ and a 2σ LJ that occurs >60 min before a hail event is called an invalid LJ or a false alarm. A hail event predicted by at least one valid LJ is called a hit, and the absence of a 2σ LJ up to 60 min before a hail event is called a miss.

3.2. HC method

The HC method based on the fuzzy logic algorithm applied in this paper requires four radar variables (Z_H , Z_{DR} , K_{DP} , and ρ_{HV}) and the sounding temperature profile. The scheme parameters mainly refer to Feng (2018) and were developed on the basis of previous research (Zrníc et al., 2001; Park et al., 2009; Dolan and Rutledge, 2009; Snyder et al., 2010). Since the original parameters of Feng (2018) are aimed at the X-band, the membership function parameters of K_{DP} are converted according to the wavelength ratio of the S-band to the X-band. The final number of output HC types is 11, including drizzle (DR), rain (RA), heavy rain (HR), rain and hail (RH), wet snow (WS), dry snow (DS), ice crystal (IC), large hail (HA), graupel and small hail (G/SH) and super-cooled water (SCW).

3.3. Method for removing false alarms

In this paper, we propose the use of particle information identified by dual-polarization radar to remove false alarms (invalid LJs). First, the sounding temperature profile and the quality-controlled radar variables (Z_H , Z_{DR} , K_{DP} , and ρ_{HV}) are used to calculate the polar coordinates of particles identified through the volume scan at nine elevations. Then, the particles identified in each elevation through volume scan are assigned to the grid points with a horizontal spacing of $1 \text{ km} \times 1 \text{ km}$ using the nearest neighbor interpolation method, and the horizontal Cartesian coordinates of the particles at each horizontal grid point at the nine elevations are obtained. That is, the polar coordinates (radial distance, azimuth, elevation) are interpolated into horizontal Cartesian coordinates (X, Y, elevation) at different elevations. In this way, each elevation has the same horizontal resolution for convenience of statistical analysis.

Four types of particles (HA, G/SH, IC, and RH) related to hail events are selected for further statistical analysis. The distributions of the four types of particles are calculated separately. For example, if a grid point at one of the nine elevations is identified as an HA particle, then the grid point is marked HA. Similarly, the distributions of G/SH particles, IC particles, and RH particles are identified at each grid point. If none of the above four types of particles are identified at the same grid point at the nine elevations, the grid point is marked as nonice. Then, the numbers of HA, G/SH, IC, and RH grid points in the hail-producing cell at a certain radar time can be separately calculated based on the single-cell identification results.

Subsequently, the variations in the five variables (rate, FD, rate2, SD and FD_rate) of the HA, G/SH, IC, or RH grid point number with time are calculated: the ratio of the HA, G/SH, IC, or RH grid point number at the next moment to that at the previous moment is called the rate; the first derivative of the number of HA, G/SH, IC, or RH grid points respect to time is called the first derivative (FD); the rate of the ratio of the HA, G/SH, IC, or RH grid point number at the next moment to that at the previous moment is called rate2; the second derivative of the HA, G/SH, IC, or RH grid point number with respect to time is called the second

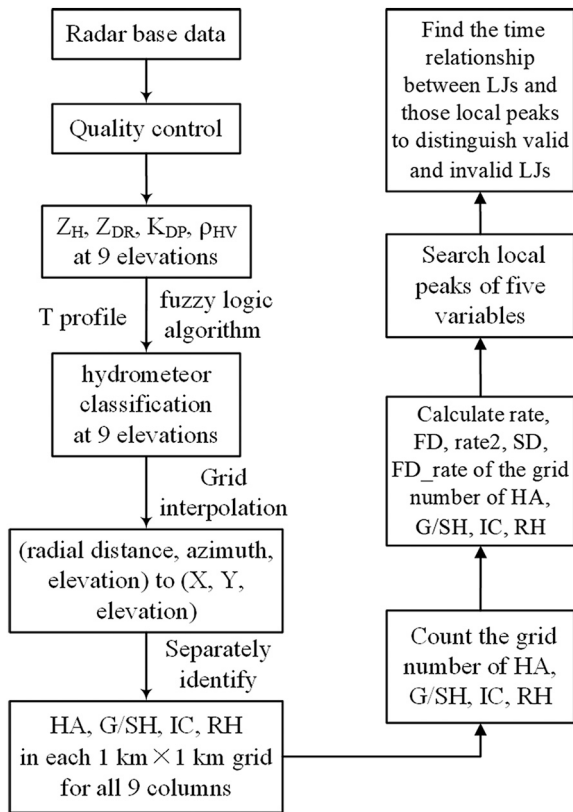


Fig. 2. Flow chart of invalid lightning jump (LJ) identification.

derivative (SD); and the ratio of the FD at the next moment to the FD at the previous moment is called the rate of FD (FD_rate). Finally, the temporal relationships between the valid and invalid LJs and the local peaks of the variations of these five variables are analyzed separately and used to remove the false alarms (invalid LJs). The entire process is

shown in Fig. 2.

4. Results

We analyzed a single hail event produced by a relatively weak convective cell on April 29, 2021, and the multiple hail events (maximum hail diameter of 50 mm) produced by a strong multicell thunderstorm on April 30, 2021.

4.1. Occurrence of an isolated cell on April 29, 2021

Due to the influence of a northeast cold vortex, strong convective weather, such as thunderstorms and hail, occurred in some areas of Huaiyin District, Huai'an City, Jiangsu Province, at 16:00–19:48 on April 29, 2021, with a maximum wind speed of 24.4 m/s. The hail event occurred at 18:16 and lasted for 1 min. The maximum hail diameter was 5 mm. This event is Case 2 in Table 1.

Fig. 3 shows the composite radar reflectivity of the multicell thunderstorms (including an isolated cell) at four time points (16:18, 17:48, 18:12, and 18:54) before and after the hail event on April 29, 2021 and the superposition results of the strong convective cells identified by the TITAN algorithm and CG flashes at the corresponding time points. At 16:18, a hail-producing cell had just formed near Suqian City, Jiangsu Province. The area of this cell was very small as evidenced by the TITAN algorithm. The cell produced four negative CG flashes, as shown in Fig. 3 (e). At 17:48, the cell gradually strengthened and expanded. Between 17:45 and 17:51, the cell produced 16 negative CG flashes. The hail-producing cell reached the maximum area at 18:12 before the hail event and produced 16 negative CG flashes and one positive CG flash within 6 min from 18:09–18:15, as shown in Fig. 3(g). Hail occurred from 18:16 to 18:17. Afterward, the intensity of the cell gradually weakened. At 18:54, the hail-producing cell produced only one negative CG flash within 6 min, as shown in Fig. 3(h). The hail-producing cell dissipated after 19:48. The maximum echo intensity during the entire hail process was 60 dBZ.

Fig. 4 shows the variation in the 2σ LJ algorithm-calculated FR and the time rate of change of the total flash rate (DFRDT) of the lightning activity generated by the hail-producing cell over time. The average FR

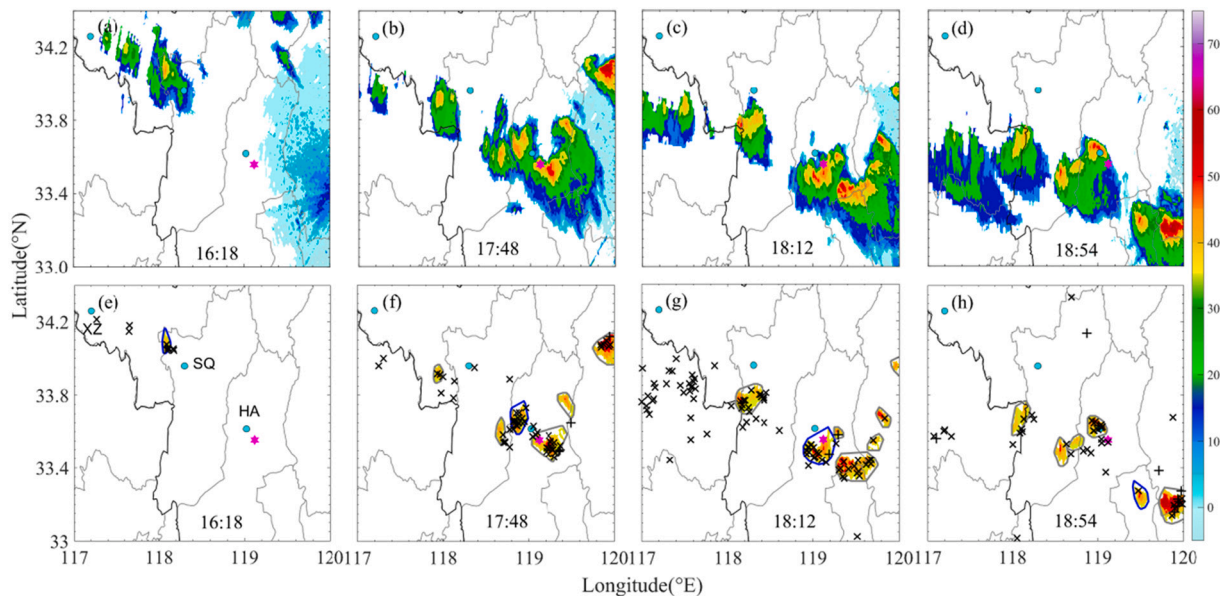


Fig. 3. Changes in the composite radar reflectivity (dBZ) at four time points (16:18, 17:48, 18:12, and 18:54) before and after hail events in Huaiyin District, Huai'an City on April 29, 2021, and changes in the superposition results of the strong convective cells identified by the TITAN algorithm and CG flashes at the corresponding time points. The light blue dots mark the prefecture-level cities in Jiangsu Province, with XZ, SQ, and HA representing Xuzhou City, Suqian City, and Huaian City, respectively; the magenta stars represent the hail locations. Positive CG flashes are represented by black “+” symbols, and negative CG flashes are represented by black “x” symbols. (For interpretation of the references to colour in this figure legend, the reader is referred to the web version of this article.)

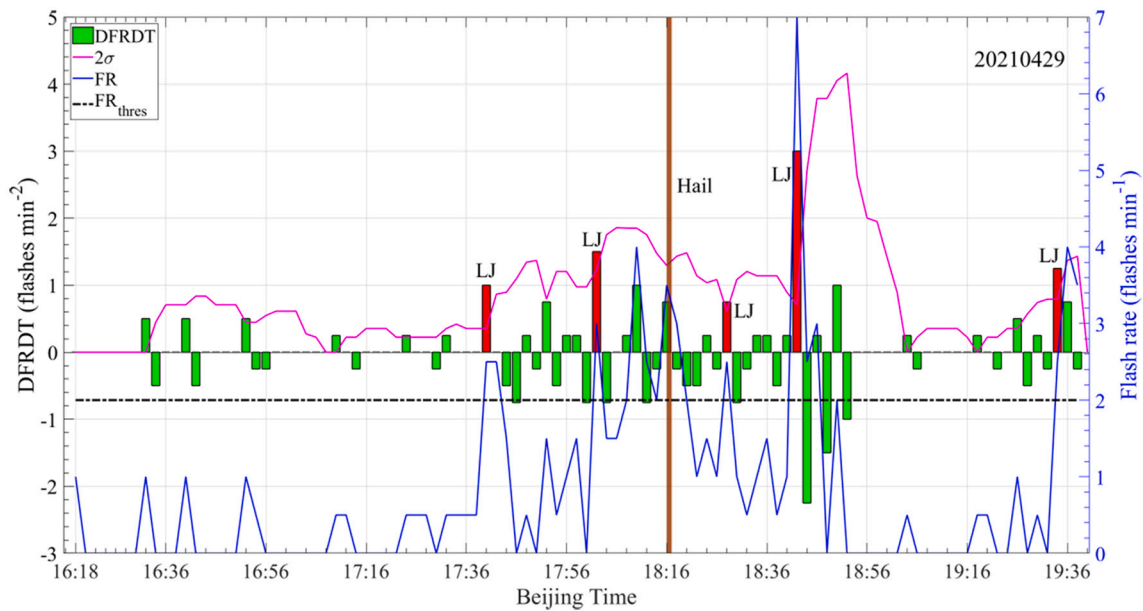


Fig. 4. The time rate of change of the total flash rate (DFRDT) and the variation in flash rate (FR) with time during the hail event (Case 2) on April 29, 2021. The pink curve represents the variation in the 2σ value with time; the blue solid line represents the variation in FR with time; the green and red bars represent the DFRDT values below and above the 2σ threshold, respectively; the black dotted line represents the FR threshold; and the brown bar indicates the duration of the hail event (the same symbols are used in Fig. 12). (For interpretation of the references to colour in this figure legend, the reader is referred to the web version of this article.)

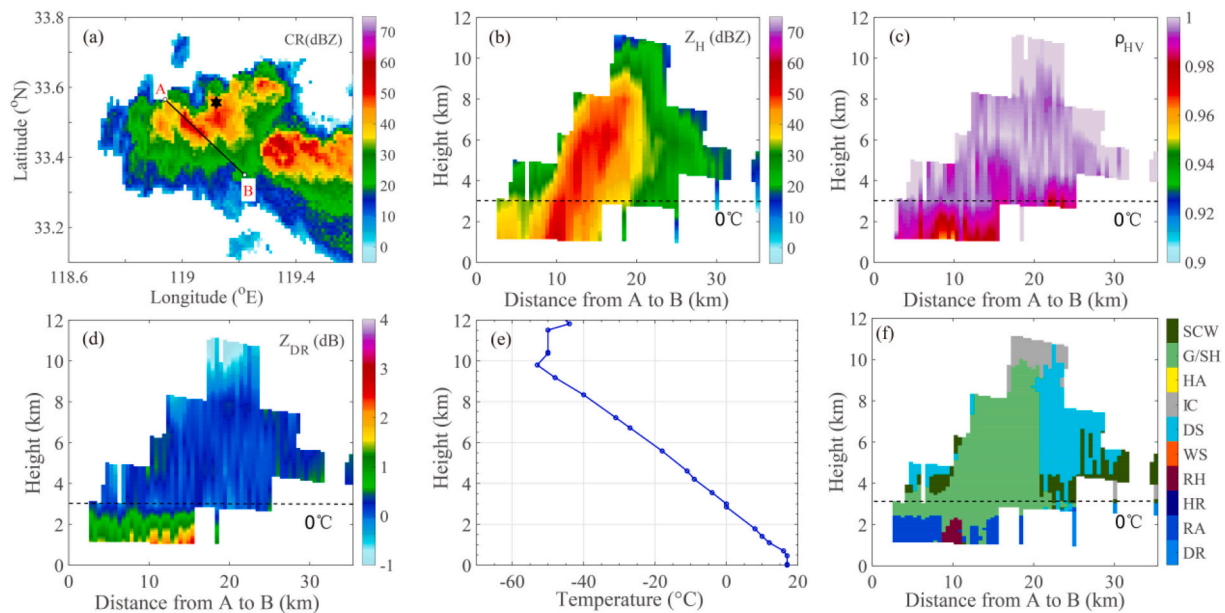


Fig. 5. (a) Schematic diagram of the location of the vertical section of the hail-producing cell, (b) Z_{DR} , (c) ρ_{HV} , (d) Z_H , (e) the vertical temperature profile observed at the Yancheng sounding station at 20:00, and (f) hydrometeor classification results. The black star represents the hail location (same for Fig. 13).

during the hail process was 0.8 flashes/min, and the maximum FR reached 8 flashes/min. The ratio of positive to negative CG flashes generated by the hail-producing cell was 15:146 (approximately 1:10). Based on the actual hail observation data, two LJ warnings before hail events (17:40 and 18:02) were valid, and three LJ warnings after hail events (18:28, 18:42 and 19:34) were invalid (false alarms).

An interpolated vertical section was selected to demonstrate the vertical structure of the hail cloud (Fig. 5) at 18:12 on April 29th, 2021, earlier than the local hail event. The composite reflectivity and the horizontal location of selected vertical section are shown in Fig. 5(a). Slantwise convection and hanging echo characteristics can be seen in Fig. 5(b), basically matching the typical features of hail-related storm

cells. There were relatively small value areas of Z_{DR} and ρ_{HV} . (Figs. 5(c), (d)) in the lower part of the Z_H core (approximately 10 km horizontally and <3 km vertically in the section), indicating the existence of ice phase hydrometeors such as graupel and hail. The HC results (Fig. 5(f)) showed a hail and rain area in the lower part that evolved from graupel falling and melting. The sounding temperature profile near the station is shown in Fig. 5(e), and the 0°C layer height was approximately 3 km.

The vertical temperature profile obtained by sounding (Fig. 5(e)) and the results of each polarization parameter were used to identify different types of hydrometeor particles at the first elevation. The distribution of these particles in various strong convective cells was then determined using the TITAN algorithm. In this way, different types of hydrometeor

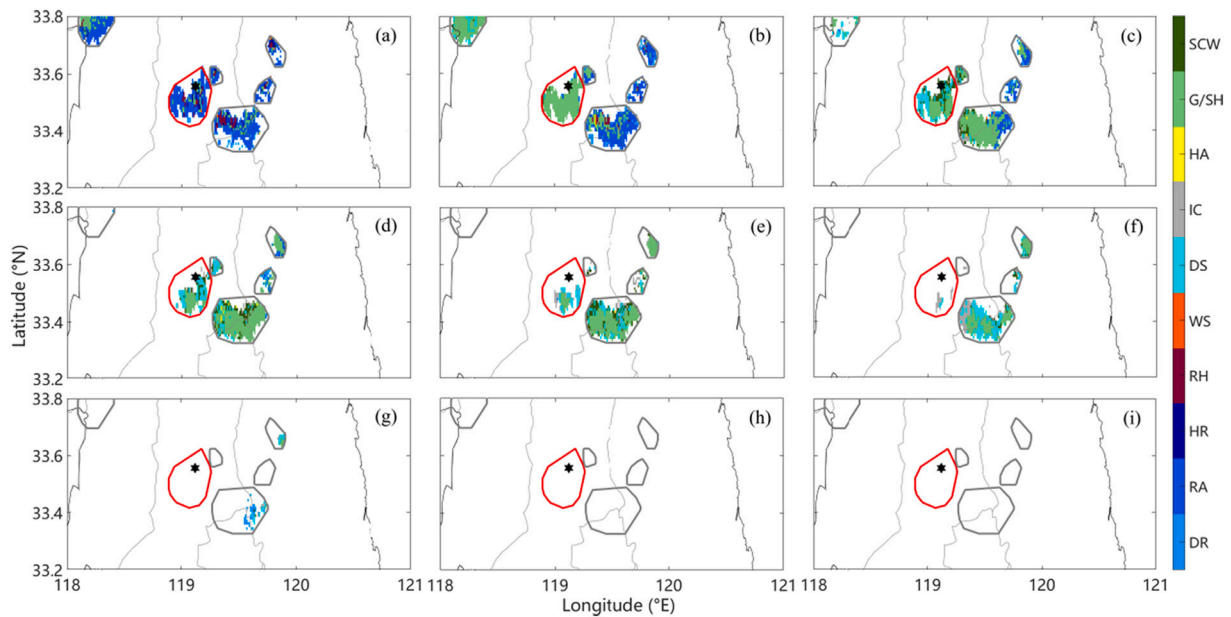


Fig. 6. Hydrometeor classification results at each elevation at 18:12. (a) First elevation, (b) second elevation, (c) third elevation, (d) fourth elevation, (e) fifth elevation, (f) sixth elevation (G) seventh elevation, (h) eighth elevation, and (i) ninth elevation. The red circles represent the hail-producing cells, and the black stars represent the hail locations. (For interpretation of the references to colour in this figure legend, the reader is referred to the web version of this article.)

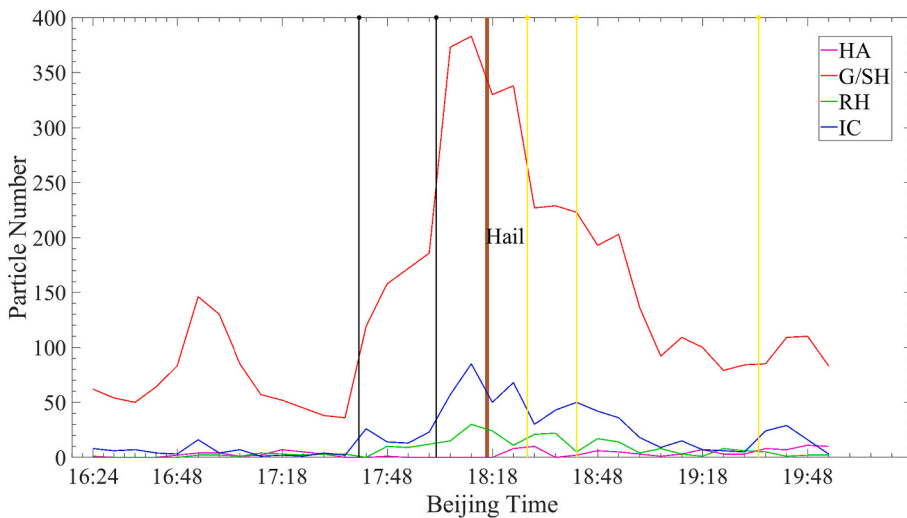


Fig. 7. Changes in the number of large hail (HA), graupel and small hail (G/SH), rain and hail (RH), and ice crystal (IC) grid points in the strong convective cell that produced the hail event. The black vertical lines represent the occurrence times of the valid LJs; the yellow vertical lines represent the occurrence times of the invalid LJs (false alarms); and the brown bar indicates the duration of the hail event (the same symbols are used in Figs. 8 and 15). (For interpretation of the references to colour in this figure legend, the reader is referred to the web version of this article.)

particles were identified at the nine elevations, and the results are shown in Fig. 6. Fig. 6(a) shows that at 18:12, three types of particles (RA, RH, and G/SH) were mainly observed in the hail-producing cell at the first elevation of the radar, with descending order of $RA > G/SH > RH$. The particles observed in the hail-producing cell at the second elevation were mostly G/SH particles, including a very small number of SCW, RA and HR particles, as shown in Fig. 6(b). Three types of particles (DS, G/SH, and SCW) were mainly observed at the third and fourth elevations, as shown in Fig. 6(c) and Fig. 6(d). Fig. 6(e) shows that the hail-producing cell also contained some IC particles. The top of the hail-producing cell might be detected by radar scan at the sixth elevation, but fewer particles (mainly IC and DS particles) were identified at this elevation. Fig. 6(g), (h) and (i) show that no hydrometeor particles were identified at the seventh, eighth or ninth elevations of the radar, indicating that the height detected at these elevations exceeded the height of the hail cloud top.

The numbers of HA, G/SH, RH and IC grid points in the hail-

producing cell at 18:12 were calculated to be 0, 330, 24, and 50, respectively, using the correlation method in Section 3.3 and the HC results from the first elevation to the ninth elevation. Fig. 7 shows the evolution of the HA, G/SH, RH and IC grid point numbers during the lifetime of the strong convective cell that generated this hail event. Throughout the lifetime of the strong convective cell, the number of G/SH grid points was far greater than those of HA, RH or IC grid points, where the number of IC grid points ranked second, and the number of HA grid points was smallest. In the early development stage of the strong convective cell, the number of HA, RH or IC grid points was always at a low level. Starting from 17:36, the number of G/SH grid points and the number of IC grid points increased rapidly. At 17:40, the first LJ occurred. At 18:00, the G/SH and IC grid points experienced a second rapid increase. At 18:02, the second LJ occurred. A rapid increase in the numbers of G/SH and IC grid points in a thunderstorm cloud increases the probability of collision between particles. Under the noninductive electrification mechanism, lightning activity is enhanced, and thus, the

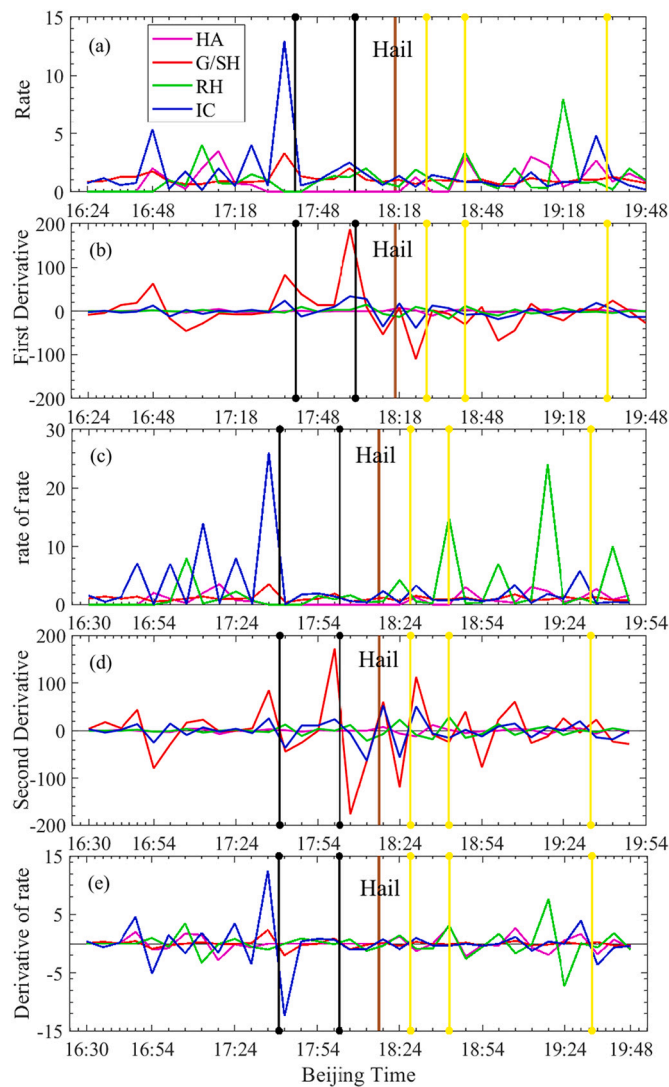


Fig. 8. Variations in the number of large hail (HA), graupel and small hail (G/SH), rain and hail (RH) and ice crystal (IC) grid points with time, (a) rate, (b) FD, (c) rate², (d) SD, and (e) FD_{rate}. The magenta line represents the HA particles; the red line represents the G/SH particles; the green line represents the RH particles; the blue line represents the IC particles. (For interpretation of the references to colour in this figure legend, the reader is referred to the web version of this article.)

FR increases rapidly. At 18:12, the numbers of G/SH, IC, and RH grid points all reached their peaks, which were 383/6 min, 85/6 min, and 30/6 min, respectively, followed by a hail event. The number of HA grid points was relatively low throughout the whole process. Interestingly, when the numbers of G/SH, IC, and RH grid points decreased, LJs occurred, but no hail event occurred following these LJs.

Fig. 8 shows the variations in the five variables (i.e., rate, FD, rate², SD and FD_{rate} mentioned in Section 3.3) of the HA, G/SH, RH and IC grid point numbers with time in this hail process. Fig. 8 shows that within 6 min (including 6 min) before the two valid LJs, positive local peaks (must be positive) occurred in the five variables of the G/SH and IC grid point numbers. However, no positive local peaks in the variations of the five variables of the G/SH grid point number occurred up to 6 min before an invalid LJ. Therefore, the positive local peaks in the variations of the five variables of the G/SH grid point number can be used to distinguish valid and invalid LJs in this case. Removing all invalid LJs (false alarms) can reduce the FAR.

4.2. Multiple hail events on April 30, 2021

Thunderstorms, hail, and rare extreme thunderstorms and gales occurred in Jiangsu Province from north to south due to a northeast cold vortex at approximately 17:00 on April 30, 2021. Hail with a maximum diameter of 50 mm and a level 13 gale with a maximum speed of 36.2 m/s were observed at the Huai'an observation station. The analysis of the evolution process of this hail-producing cell showed that Cases 6, 7, 8, 9, 11 and 12, which occurred on the same day, were produced by the same hail-producing cell. Table 2 shows that the smallest maximum hail diameter in this strong convection process was 10 mm and that the maximum hail diameter in case 8 reached 35 mm.

Fig. 9 shows the composite radar reflectivity near the occurrence times of the six hail events. The six hail events were all located at the boundary of the strong convective cell but not at the center of the strong convective cell. The strongest composite reflectivity of the hail-producing cell exceeded 60 dBZ at all six time points and exceeded 65 dBZ at 18:30, as shown in Fig. 9(c).

Fig. 10 shows the strong convective cells near the occurrence times of the six hail events identified by the TITAN algorithm. It can be seen more clearly that the hail location was not at the center of the strong convective cell.

Fig. 11 shows that the CG lightning activity is relatively consistent with the strong convective cells identified by the TITAN algorithm. A total of 5251 (90.6%) negative CG flashes and 543 positive CG flashes (9.4%) were detected during the development of the strong convective cell that produced the six hail events, and the number of negative CG flashes was much larger than that of positive CG flashes.

Fig. 12 shows the changes in the FR and DFRDT of the lightning activity generated by the strong convective cell in this process, and Table 3 shows the corresponding valid and invalid LJs. The average FR during the hail process was 17.4 flashes/min, and the maximum FR reached 46 flashes/min. The ratio of positive to negative CG flashes generated by the hail-producing cell was 543:5251 (approximately 1:10). In this case, the FR threshold used to calculate the LJs was also set to 2. Of the nine LJs generated in this thunderstorm, seven were valid, and two were invalid. As no hail events occurred within 60 min after the LJs at 17:10 and 19:52, the two LJs were classified as invalid LJs (false alarms). The early warning based on the remaining valid LJs resulted in the lead times of 58 min, 28 min, 44 min, 60 min, 34 min, and 45 min for the six hail events, indicating that the 2 σ LJ algorithm was able to predict the six hail events in an average of 44.8 min in advance.

An interpolated vertical section at 18:12 before the hail event is shown (Fig. 13). The composite reflectivity and the horizontal location of the selected vertical section are shown in Fig. 13(a). With the case of April 29th, 2021, in the previous section, in addition to the similar slantwise convection and hanging echo features, this cell had higher reflectivity and a core over 65 dBZ at approximately 4 km height (Fig. 13(b)). A negative Z_{DR} and relatively small ρ_{HV} were found for the Z_H core area (Figs. 13(c), (d)), indicating that large ice phase particles existed. The HC results showed a wide forward leaning area of hail (Fig. 13(f)) below 6 km. This result was consistent with the ground observation that the hail size was much greater than that on April 29, 2021. Since all six hail events occurred at nightfall and were close to the Yancheng sounding station, the sounding data from Yancheng station at 20:00 April 30th 2021, were selected, as shown in Fig. 13(e), and the 0 °C layer height was approximately 2.6 km.

The HC results of the cell producing six hail events at the first elevation were obtained based on the quality-controlled radar polarization parameters and the sounding data (Fig. 13(e)), as shown in Fig. 14. Fig. 14(a) shows that the center of the hail-producing cell was mainly composed of RH and HA particles, which covered the hail location, while the periphery of the lower part of the hail-producing cell was mainly composed of RA particles. The cell producing Case 7 was divided into two connected parts on the left and right, with the same particle distributions, i.e., HA and RH particles at the center, G/SH

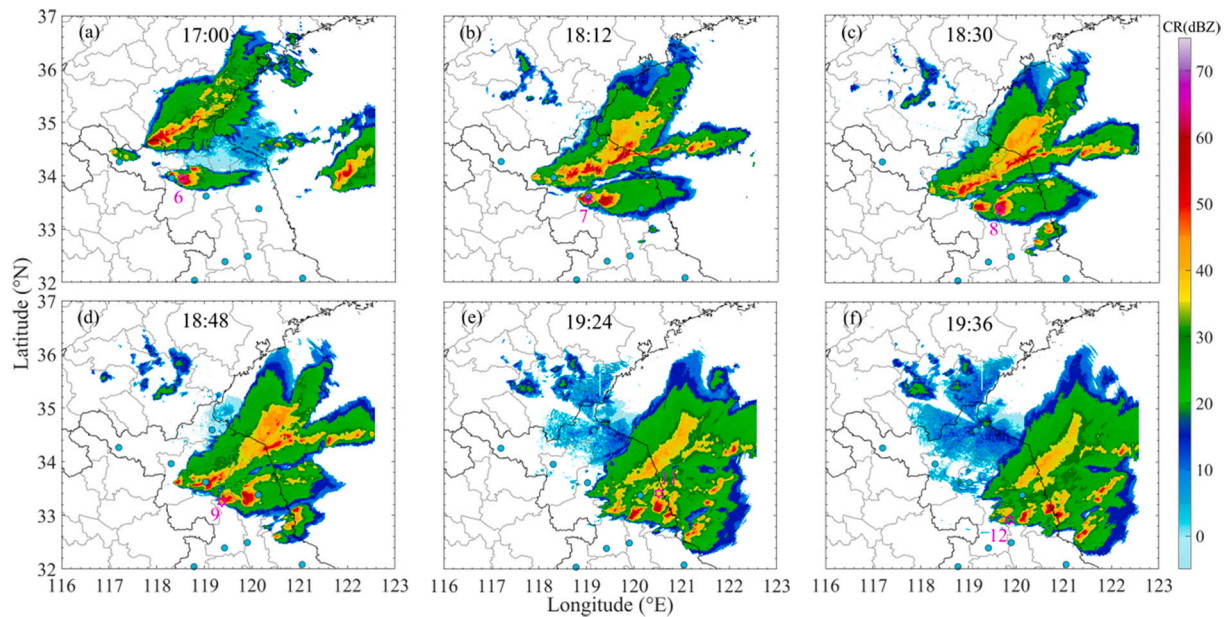


Fig. 9. Composite radar reflectivity results near the occurrence times of the six hail events on April 30, 2021. The magenta stars mark the hail locations, and each hail event is assigned to a case number (same for Figs. 10 and 11). (For interpretation of the references to colour in this figure legend, the reader is referred to the web version of this article.)

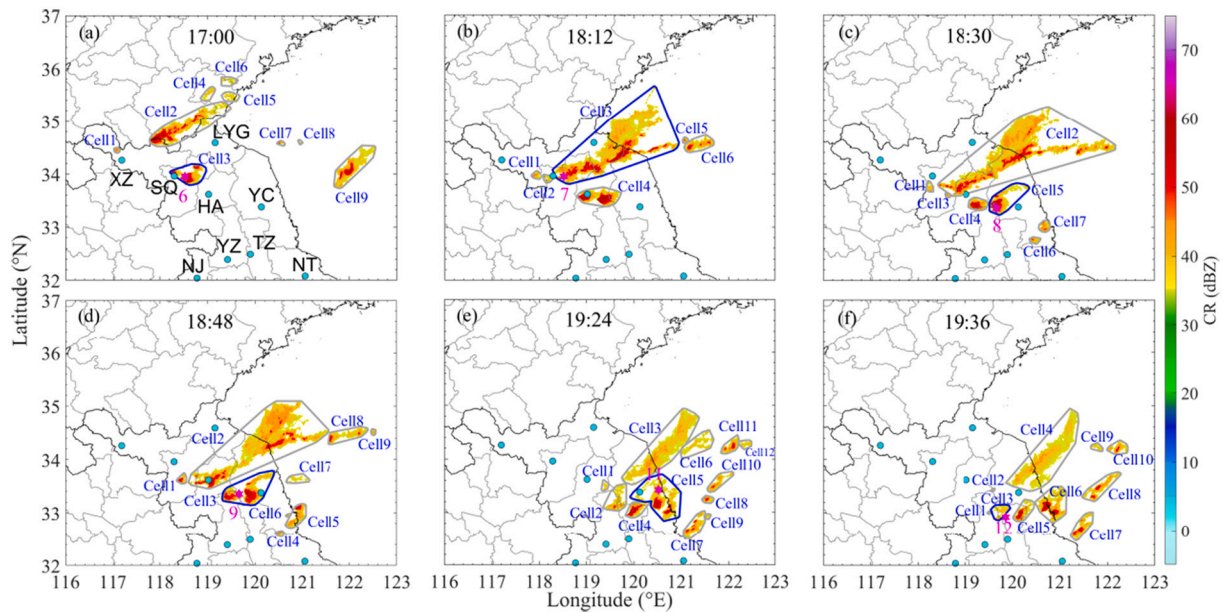


Fig. 10. The strong convective cells near the occurrences of the six hail events identified by the TITAN algorithm on April 30, 2021. The blue polygon surrounds the hail-producing strong convective cell. LYG, YC, NJ, YZ, TZ, and NT represent Lianyungang, Yancheng, Nanjing, Yangzhou, Taizhou, and Nantong, respectively. (For interpretation of the references to colour in this figure legend, the reader is referred to the web version of this article.)

particles in the middle, and RA and DR particles at the outermost part, as shown in Fig. 14(b). In contrast, the center of the cell producing Case 8 was mainly composed of HA particles. A strong hail process with a maximum hail diameter of 35 mm was observed at the southern boundary of these HA particles. HA, G/SH mixed with RH, and RA particles were distributed at the center, middle and outermost parts of the cell, respectively. Case 9 was located in the left half of the hail-producing cell, and the RA particles distributed in the outermost part of the lower part of the cell enclosed HA, RH, and G/SH particles and a small number of WS particles, as shown in Fig. 14(d). The cell producing Case 11 had a relatively large area. Although the hydrometeor particles

in the sky above the hail location were mostly G/SH particles, sometimes the HA particles identified in the thunderstorm cloud did not necessarily fall to the ground. In addition, the maximum diameter of HA particles in Case 11 was 9 mm, which was the smallest of the six hail events. Therefore, the hydrometeor particles falling to the ground in Case 11 might have been G/SH particles. Fig. 10(f) shows that Case 12 was located in the weak convection area of the hail-producing cell, and therefore, the hail location was outside the strong convective cell (the area inside the magenta circle). The HC results showed that the lower part of this cell was dominated by G/SH particles, which is consistent with the relatively small maximum hail diameter observed (10 mm). In

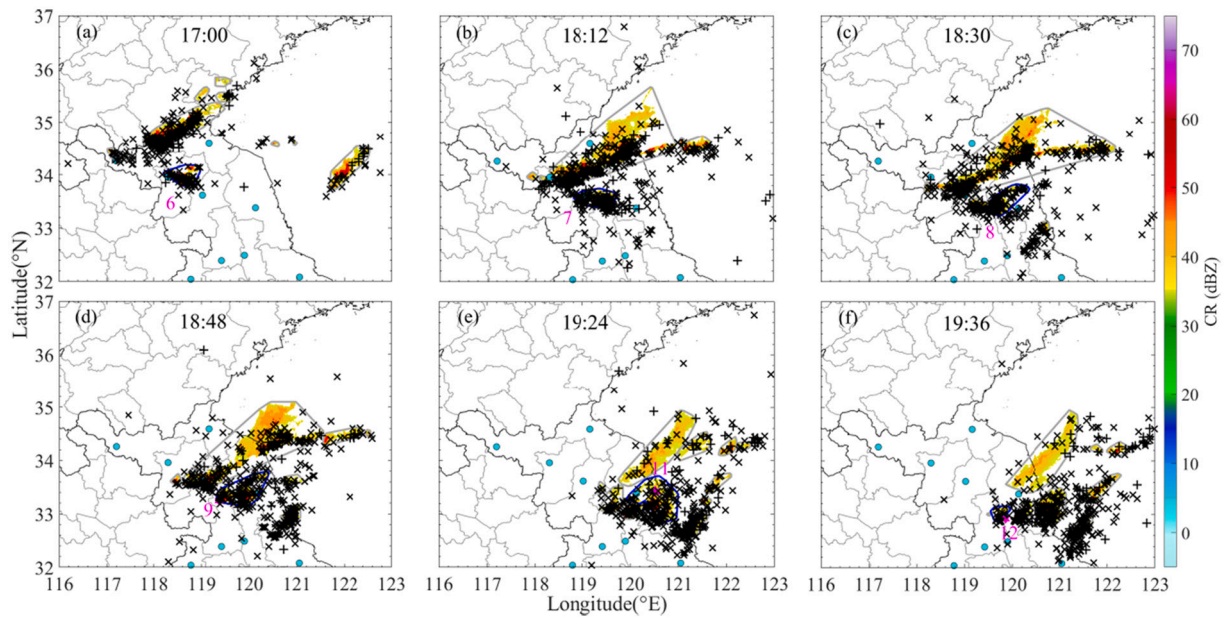


Fig. 11. The superposition results of the strong convective cells identified by the TITAN algorithm and CG flashes at the corresponding time points on April 30, 2021.

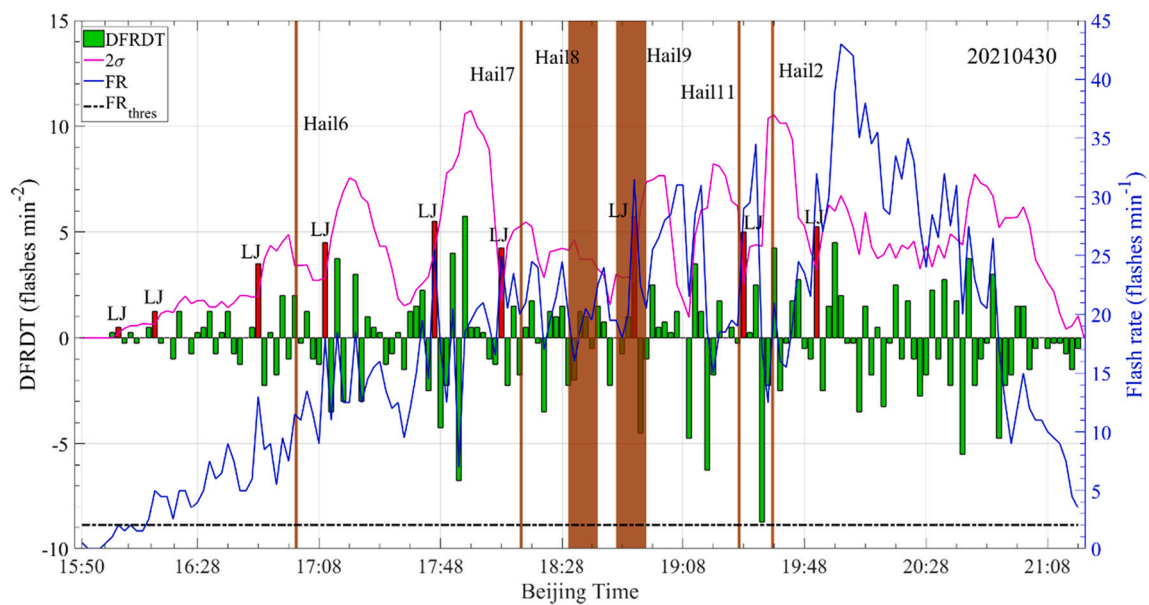


Fig. 12. Changes in FR and DFRDT during Cases 6, 7, 8, 9, 11 and 12 on April 30, 2021.

Table 3
Statistics of the lightning jumps (LJs) in Cases 6, 7, 8, 9, 11 and 12 on April 30, 2021.

Occurrence time(s) of LJ (Beijing time)	Duration of hail events predicted by LJ	Valid or invalid LJs	Lead time (min)
16:02, 16:14, 16:48	17:00-unrecorded	Valid	58
17:46, 18:08	18:14-unrecorded	Valid	28
	18:30-18:40		44
	18:46-18:56		60
18:52	18:46-18:56	Valid	NA
	19:26-unrecorded		34
	19:37-unrecorded		45
19:28	19:37-unrecorded	Valid	NA
17:10	NA	Invalid	NA
19:52	NA	Invalid	NA

summary, the resulting hail diameter is relatively large (>15 mm) if the lower part of a thunderstorm cell above the hail location is dominated by HA particles, while the resulting hail diameter is small (approximately 10 mm) if the lower part of a thunderstorm cell above the hail location is dominated by G/SH particles.

Fig. 15 shows the evolution of the HA, G/SH, IC, and RH grid point numbers during the lifetime of the strong convective cell that produced the six hail events. Throughout the lifetime of the strong convective cell, there were considerably more G/SH grid points than HA, IC, and RH grid points and very few HA and RH grid points. At 15:48, a strong convective cell was formed. The cell contained 50 G/SH grid points, three IC grid points, one HA grid points, and one RH grid point. Subsequently, the number of G/SH grid points increased rapidly, while the numbers of HA, IC, and RH grid points did not change much. At the same time, two LJs occurred. Prior to Case 6, the numbers of all four types of particles increased rapidly in a short time, and another LJ occurred. All three LJs

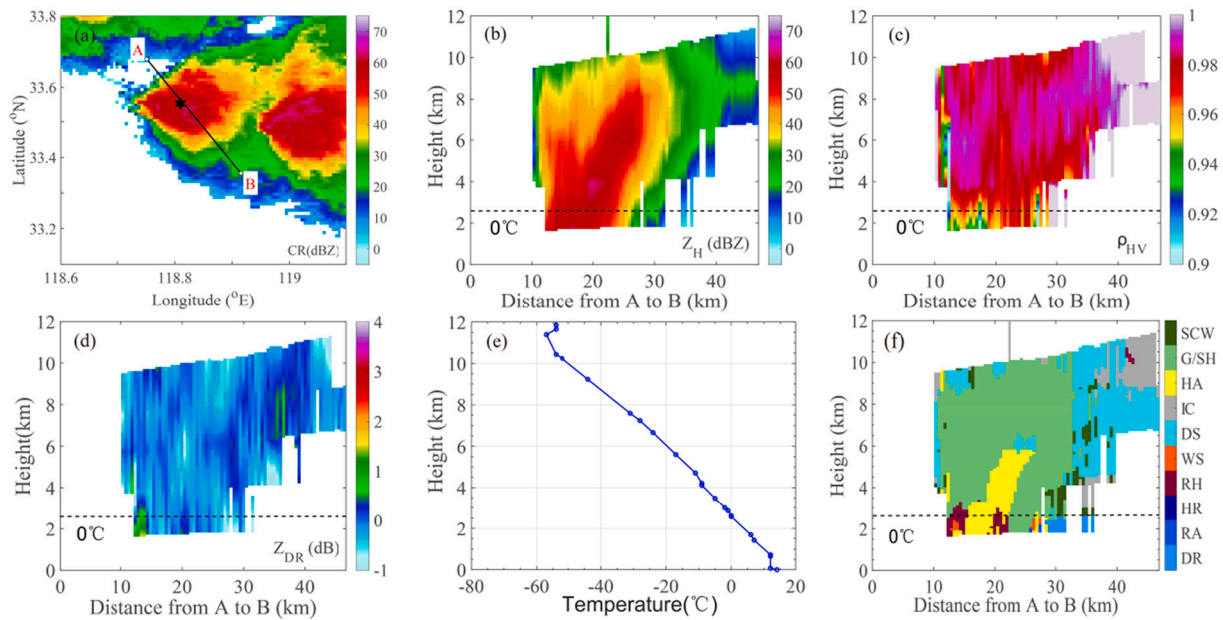


Fig. 13. (a) Schematic diagram of the location of the vertical section of the hail-producing cell, (b) Z_{DR} , (c) ρ_{HV} , (d) Z_H , (e) the vertical temperature profile observed at the Yancheng sounding station at 20:00, (f) hydrometeor classification results.

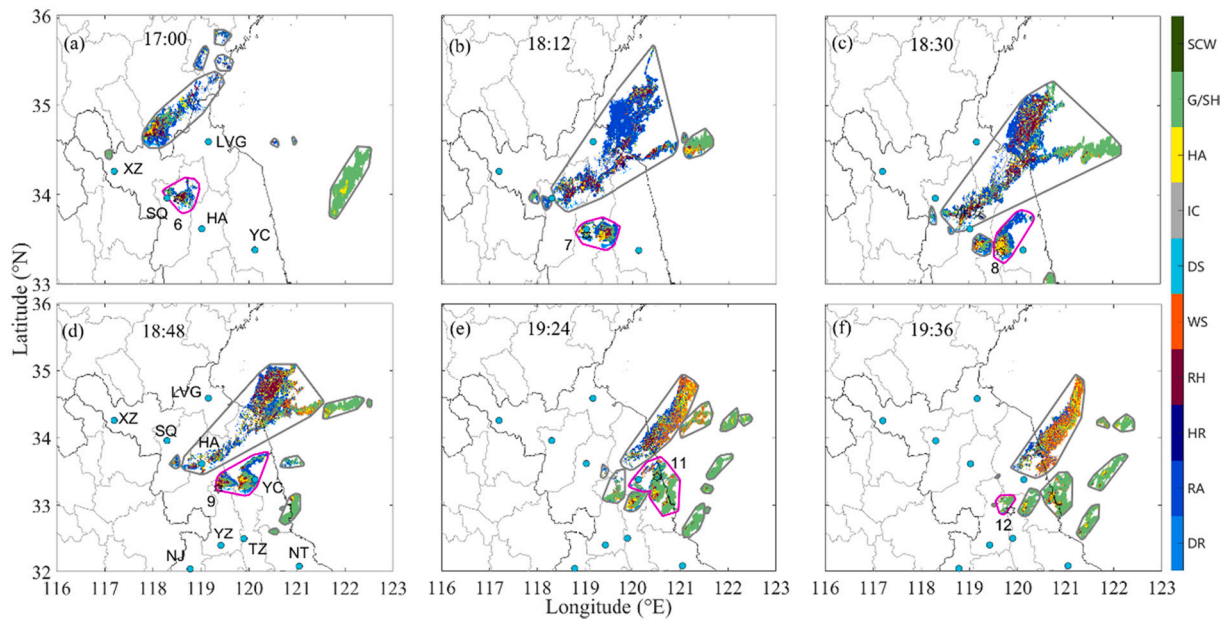


Fig. 14. Hydrometeor classification results at the first elevation for the six hail events. The gray circles represent the identified strong convective cells; the magenta circles represent the hail-producing cells; the black stars represent the hail locations. (For interpretation of the references to colour in this figure legend, the reader is referred to the web version of this article.)

were valid. Prior to Case 7, the number of G/SH grid points persistently increased, and three LJs occurred, with the earliest LJ being invalid. It is worth noting that the number of G/SH grid points and the number of IC grid points decreased briefly after the hail event, indicating that this hail event may have been formed by G/SH and IC particles. Within 48 min before and after the occurrence of Cases 8 and 9, the number of G/SH grid points in the strong convective cell increased rapidly, the number of IC grid points increased, and the number of HA and RH grid points did not change much. After the occurrence of Case 11, a valid LJ occurred. In addition, the number of G/SH grid points and the number of IC grid points reached peak values of 3415/6 min and 1626/6 min, respectively. Interestingly, Case 12 occurred when the numbers of HA, G/SH, IC, and

RH grid points were decreasing. Subsequently, the number of G/SH grid points in the cell increased rapidly again, and an LJ occurred but was invalid (the LJ was a false alarm).

Fig. 16 shows the variation in the five variables of the HA and G/SH grid point numbers with time in the six hail events. Fig. 16(a) shows that, except for the last valid LJ, positive local peaks occurred in the rate of the HA or G/SH grid point number within 6 min before all the other valid LJs. Based on the results presented in Table 3, the valid LJ at 18:52 can be used to predict the last two hail processes, such that the removal of the last valid LJ does not affect the POD. The first invalid LJ could be removed because no positive local peaks occurred in the rate of the HA and G/SH grid point number within 6 min before this LJ. The second

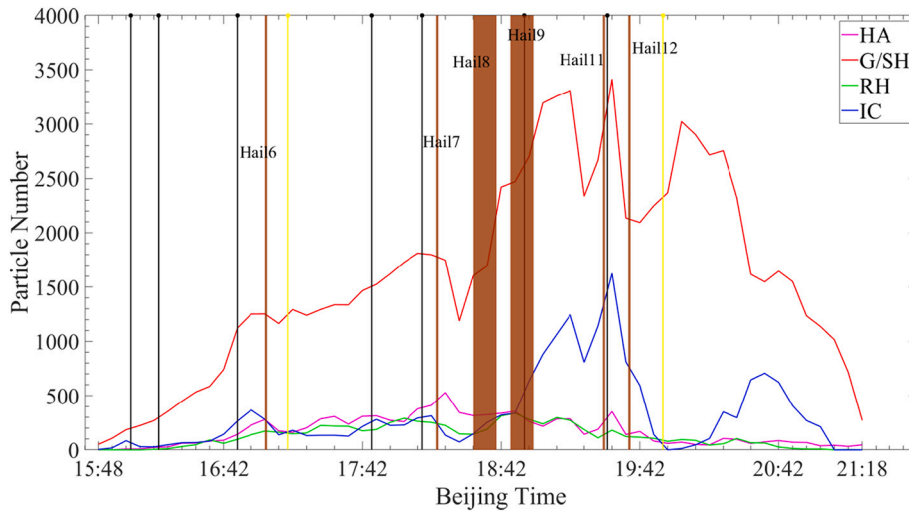


Fig. 15. Changes in the numbers of large hail (HA), graupel and small hail (G/SH), ice crystal (IC), and rain and hail (RH) grid points in the strong convective cell that produced the six hail events over time.

invalid LJ could not be removed because a positive local peak in the rate of the G/SH grid point number occurred within 6 min before this LJ. The evaluation result of each LJ based on FD was consistent with that based on rate, as shown in Fig. 16(b). The start time of rate2, SD or FD_rate was 6 min later than that of rate or FD because the number of grid points was processed twice. Fig. 16(c) shows that positive local peaks occurred in rate2 of the HA or G/SH grid point number within 6 min before all valid LJs except the first valid LJ. Similarly, based on Table 3, removing the first valid LJ did not affect the early warning of Case 6. More importantly, no positive local peaks occurred in rate2 of the HA or G/SH grid point number 6 min before the two invalid LJs, such that both LJs could be removed. The evaluation result of each LJ based on SD (Fig. 16(d)) was consistent with that based on rate2. Although all invalid LJs identified based on FD_rate, such as those identified based on rate2, could be removed, the second to last LJ identified based on FD_rate could also be removed because no positive peaks occurred in FD_rate of the HA and G/SH grid point number 6 min before this valid LJ, as shown in Fig. 16(e). In addition, based on Table 3, Cases 11 and 12 could not be predicted after the valid LJ at 18:52 was removed. In summary, rate2 and SD performed the best in this hail process.

4.3. Comparison of the identification of valid and invalid LJs in 17 cases

Through the statistical analysis of a total of 17 hail cases on April 29 and 30, 2021, we compared the numbers of valid and invalid LJs correctly and incorrectly identified based on the comprehensive consideration of the five variables of the HA and G/SH grid point numbers, as shown in Fig. 17. As shown in Fig. 17(a), the highest number (22) of correctly identified valid LJs was obtained based on FD, the lowest number (17) of correctly identified valid LJs was obtained based on FD_rate, the number of correctly identified valid LJs obtained based on rate2 or SD was 20, and the number of correctly identified valid LJs obtained based on rate was 21. The highest number of correctly identified invalid LJs (16 times) was obtained based on rate2 or FD_rate, the number of correctly identified invalid LJs obtained based on rate or SD was 13, and the number of correctly identified invalid LJs obtained based on FD was 14. As shown in Fig. 17(b), the lowest number (7) of incorrectly identified valid LJs was obtained based on FD, and the lowest number (7) of incorrectly identified invalid LJs was obtained based on rate2. Note that for the 17 cases analyzed in this paper, multiple valid LJs usually occur before a hail event; if one or two valid LJs are removed or erroneously identified, the remaining correctly identified valid LJs can still provide an early warning for the hail event, where the number

of hits remains unchanged. In summary, rate2 does not affect the effective early warning of hail events, and it has the highest efficiency of identifying invalid LJs, approximately 69.6% (16/23), and a moderate false identification rate for valid LJs, 31.0% (9/29).

4.4. Evaluation of the performance of the 2σ LJ algorithm before and after removing invalid LJs

Table 4 shows the hail warning performance of the 2σ LJ algorithm for the 17 cases of hail events before and after the invalid LJs were removed. After the invalid LJs were removed, the number of hits obtained using the 2σ LJ algorithm remained unchanged, whereas the number of false alarms decreased from nine and 15 to three and four for the hail events on April 29 and 30, 2021, respectively. Before the invalid LJs were excluded, the POD of the 2σ LJ algorithm for hail warning was

$$POD = \frac{hits}{(hits + misses)} = \frac{17}{(17 + 0)} = 100\% \tag{1}$$

the FAR was

$$FAR = \frac{falses}{hits + falses} = \frac{24}{(17 + 24)} \approx 58.5\% \tag{2}$$

the critical success index (CSI) was

$$CSI = \frac{hits}{(hits + misses + falses)} = \frac{17}{(17 + 0 + 24)} \approx 41.5\% \tag{3}$$

and the average lead time was 37.9 min. After the invalid LJs were removed, the POD of the 2σ LJ algorithm for hail warning was

$$POD = \frac{hits}{(hits + misses)} = \frac{17}{(17 + 0)} = 100\% \tag{4}$$

the FAR was

$$FAR = \frac{falses}{hits + falses} = \frac{7}{(17 + 7)} \approx 29.2\% \tag{5}$$

the CSI was

$$CSI = \frac{hits}{(hits + misses + falses)} = \frac{17}{(17 + 0 + 7)} \approx 70.8\% \tag{6}$$

and the average lead time was 35.1 min. Using the proposed method slightly reduced the average lead time but considerably improved the

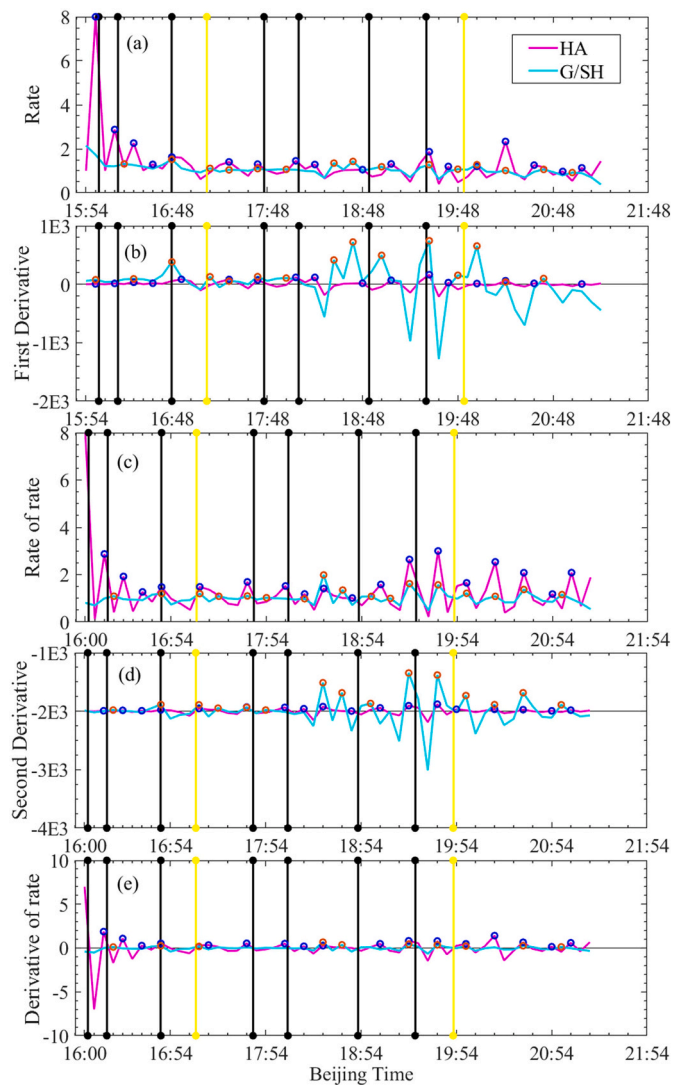


Fig. 16. Variation in the numbers of hail (HA) and graupel and small hail (G/SH) grid points with time: (a) rate, (b) FD, (c) rate2, (d) SD, (e) FD_rate. The blue circles mark the positive local peak values of the curves of HA particles; the brown circles mark the positive local peak values of the curves of G/SH particles. (For interpretation of the references to colour in this figure legend, the reader is referred to the web version of this article.)

FAR and CSI of the algorithm.

5. Conclusion and discussion

In this study, an analysis was performed on the hail warning performance of the 2σ LJ algorithm and the relationship between valid and invalid LJs and the rate, FD, rate2, SD and FD_rate of the HA, G/SH, IC, and RH grid point numbers for 17 hail events that occurred across Jiangsu Province on April 29 and 30, 2021. The analysis was based on the types of hydrometeor particles in the hail-producing cell identified by S-band dual-polarization radar and CG lightning activity. The results of this study are summarized below.

1. A method is proposed that combines the HC results of dual-polarization radar and the 2σ LJ algorithm to increase hail warning performance. For the 2σ LJ algorithm, if a positive local peak occurs in rate2 of the HA or G/SH grid point number up to 6 min before an LJ, then the LJ is valid. Otherwise, the LJ is invalid.

2. This method can effectively remove the invalid LJs in hail warnings in the 2σ LJ algorithm, with a rejection rate of 69.6% and a moderate false identification rate of 31.0% (9/29) for the valid LJs.
3. Compared with the conventional 2σ LJ algorithm, using the proposed method results in the same number of hits (17) and a reduction in the number of false alarms from 24 to 7. The POD for hail warning remain unchanged at 100%, the FAR decreases from 58.5% to 29.2%, the CSI increases from 41.5% to 70.8%, and the average lead time decreases slightly from 37.9 min to 35.1 min.
4. The hail diameter is relatively large (>15 mm) if the lower part of a thunderstorm cell above the hail location is dominated by HA particles, while the hail diameter is relatively small (approximately 10 mm) if the lower part of a thunderstorm cell above the hail location is dominated by G/SH particles.

Therefore, the method proposed in this paper can greatly improve the hail warning performance of the 2σ LJ algorithm and lays a good foundation for its practical application.

Of course, the start time of the rate2-processed data was 12 min later than the start time of the original data because the number of radar-identified grid points was processed twice. Consequently, the rate2-based method might lead to the removal of valid LJs during this period of time. However, this did not affect the final results in this paper. In addition, the results of this study must be verified by combining more hail events with total flash location data.

It is more effective to combine HC and LJ for hail warning than to apply these methods independently. Dual-polarization weather radar has surveillance capability to discriminate heavy rain and hail but is limited in terms of producing early warning of falling hail. Severe surges in the convective system usually occur during the early stage of hailing, and rapid evolution of the convective cells makes it difficult to apply time extrapolation of the HC results to accurate nowcasting. However, graupel and small hail are commonly obtained HC results during the main part of a severe convection event. Using these results in the upper-level cloud alone cannot help fully determine whether these particles will fall and melt or produce falling hail later. And the early warning time would be too short if it was based on “hail” in the HC results near ground. Therefore, it is not easy to determine indicators from HC results for precise early warning of hail falling. LJ is a clear signal that can easily be used as an early warning indicator. In the cases demonstrated in this paper, LJs occur approximately half an hour earlier than falling hail during the early stage of convective events. Removing invalid LJs based on the variations in the HC increases the reliability of the capability for early (half an hour in advance) hail warning.

In the future, we will apply this method to the X-band radar network system established by the Beijing Meteorological Bureau to verify the performance of the rate2-based method under the more accurate identification of the hydrometeor particles in the hail-producing cell at higher spatial and temporal resolutions, laying the foundation for the practical application of the rate2-based method in hail warning.

CRedit authorship contribution statement

Ye Tian: Conceptualization, Methodology, Software, Writing – original draft. **Wen Yao:** Methodology, Supervision, Writing – review & editing. **Yue Sun:** Software, Visualization, Investigation. **Yu Wang:** Data curation. **Xulin Liu:** Software, Validation. **Tao Jiang:** Software, Validation. **Longbin Zhang:** Software, Validation. **Lei Meng:** Software, Validation. **Lu Wang:** Software, Validation. **Xueqi Sun:** Data curation. **Hailong Wang:** Data curation.

Declaration of Competing Interest

The authors declare that they have no known competing financial interests or personal relationships that could have appeared to influence the work reported in this paper.

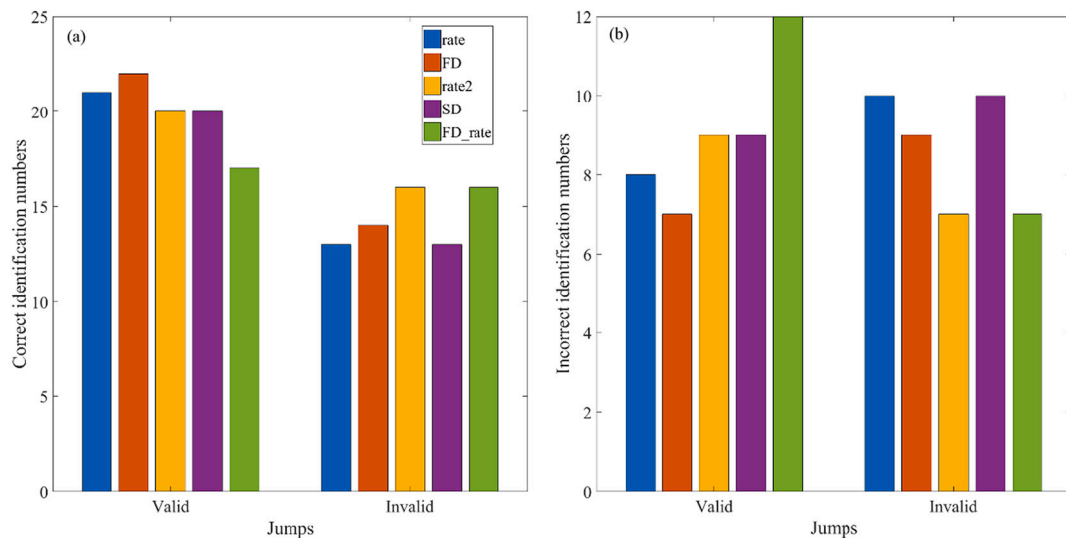


Fig. 17. Comparison of the identification of valid lightning jumps (LJs) and invalid LJs based on rate, FD, rate2, SD and FD_rate. (A) Comparison of the number of correctly identified LJs. (b) Comparison of the number of incorrectly identified LJs.

Table 4

Comparison of the performance of the 2σ LJ algorithm before and after removing invalid LJs.

Date	Before				After			
	Hits	False alarms	Misses	Lead time (min)	Hits	False alarms	Misses	Lead time (min)
20,210,429	4	9	0	51, 36, 20, 26	4	3	0	43, 36, 20, 18
20,210,430	13	15	0	16, 27, 53, 52, 35, 58, 28, 44, 60, 34, 45, 19, 40	13	4	0	16, 27, 53, 52, 21, 46, 28, 44, 60, 34, 45, 13, 40
Total	17	24	0	37.9 (avg)	17	7	0	35.1 (avg)

Acknowledgments

This study was supported by the Open Research Program of the State Key Laboratory of Severe Weather (2019LASW-B07).

References

Allen, J.T., Giammanco, I.M., Kumjian, M.R., et al., 2020. Understanding hail in the earth system[J]. *Rev. Geophys.* 58 (1), e2019RG000665.

Bang, S.D., Cecil, D.J., 2019. Constructing a multifrequency passive microwave hail retrieval and climatology in the GPM domain[J]. *J. Appl. Meteorol. Climatol.* 58 (9), 1889–1904.

Bao, Y.X., Qin, W.N., Gao, P., et al., 2012. Spatiotemporal change patterns of hail disaster in Jiangsu Province during recent 30 years[J]. *J. Nat. Dis.* 21 (05), 197–206.

Bruick, Z.S., Rasmussen, K.L., Cecil, D.J., 2019. Subtropical south american hailstorm characteristics and environments. *Mon. Weather Rev.* 147 (12), 4289–4304.

Burke, A., Snook, N., Gagne II, D.J., et al., 2020. Calibration of machine learning-based probabilistic hail predictions for operational forecasting[J]. *Weather Forecast.* 35 (1), 149–168.

Carey, L.D., Bain, A.L., Mathee, R., 2014. Kinematic and microphysical control of lightning in multicell convection over Alabama during DC3[C]. In: 5th International Conference on Lightning Meteorology, pp. 20–21.

Carey, L.D., Schultz, E.V., Schultz, C.J., et al., 2019. An evaluation of relationships between radar-inferred kinematic and microphysical parameters and lightning flash rates in Alabama storms[J]. *Atmosphere* 10 (12), 796.

Caylor, J., Chandrasekar, V., 1996. Time-varying ice crystal orientation in thunderstorms observed with multiparameter radar. *IEEE Trans. Geosci. Remote Sens.* 34 (4), 847–858. <https://doi.org/10.1109/36.508402>.

Chen, J., Wu, Y., Zhao, Z., 2010. The new lightning detection system in China: its method and performance[C]. In: Asia-Pacific International Symposium on Electromagnetic Compatibility, vol. 2010. IEEE, Beijing, China, pp. 1138–1141.

Chen, J., Zhao, C., Gu, S., et al., 2016. Present status and development trend of lightning detection and protection technology of power grid in China. *High Volt. Eng.* 42 (11), 3361–3375. <https://doi.org/10.13336/j.1003-6520.hve.20161031001>.

Chronis, T., Carey, L.D., Schultz, C.J., et al., 2015. Exploring lightning jump characteristics. *Weather Forecast.* 30 (1), 23–37.

Curtis, N., Carey, L.D., Schultz, C.J., 2018. An analysis of the lightning jump algorithm using geostationary lightning mapper flashes. In: Paper Presented at 25th

International Lightning Detection Conference and 7th International Lightning Meteorology Conference. Vaisala Inc, Ft. Lauderdale, FL.

Dixon, M., Wiener, G., 1993. TITAN: thunderstorm identification, tracking, analysis, and nowcasting—a radar-based methodology. *J. Atmos. Ocean. Technol.* 10 (10), 785.

Dolan, B., Rutledge, S.A., 2009. A theory-based hydrometeor identification algorithm for X-band polarimetric radars. *J. Atmos. Ocean. Technol.* 26 (10), 2071–2088. <https://doi.org/10.1175/2009JTECHA1208.1>.

Farnell, C., Rigo, T., 2020a. The lightning jump, the 2018 “Picking up Hailstones” campaign and a climatological analysis for catalonia for the 2006-2018 period. *J. Mediterr. Meteorol. Climatol.* 17, 10–20.

Farnell, C., Rigo, T., 2020b. The lightning jump algorithm for nowcasting convective rainfall in catalonia[J]. *Atmosphere* 11 (4), 397.

Farnell, C., Rigo, T., Pineda, N., 2017. Lightning jump as a nowcast predictor: application to severe weather events in Catalonia. *Atmos. Res.* 183, 130–141.

Feng, L., 2018. The Study of Cloud Microphysical Features of Severe Storms Based on the X-Band Dual-Polarization Radar. PH.D. Dissertation (in Chinese). Institute of Atmospheric Physics, University of Chinese Academy of Sciences, p. 117.

Gatlin, P., 2007. Severe Weather Precursors in the Lightning Activity of Tennessee Valley Thunderstorms (M.S. thesis).

Gatlin, P.N., Goodman, S.J., 2010. A total lightning trending algorithm to identify severe thunderstorms. *J. Atmos. Ocean. Technol.* 27, 3–22.

Gensini, V.A., Converse, C., Ashley, W.S., et al., 2021. Machine learning classification of significant tornadoes and hail in the United States using ERA5 proximity soundings [J]. *Weather Forecast.* 36 (6), 2143–2160.

Kalina, E.A., Friedrich, K., Motta, B.C., et al., 2016. Colorado plowable hailstorms: synoptic weather, radar, and lightning characteristics[J]. *Weather Forecast.* 31 (2), 663–693.

Kumjian, M.R., Lombardo, K., 2020. A hail growth trajectory model for exploring the environmental controls on hail size: Model physics and idealized tests[J]. *J. Atmos. Sci.* 77 (8), 2765–2791.

Laviola, S., Monte, G., Levizzani, V., et al., 2020. A new method for hail detection from the GPM constellation: a prospect for a global hailstorm climatology[J]. *Remote Sens.* 12 (21), 3553.

Liu, H.P., Chandrasekar, V., 2000. Classification of hydrometeors based on polarimetric radar measurements: development of fuzzy logic and neuro-fuzzy systems and in situ verification. *J. Atmos. Ocean. Technol.* 17 (2), 140–164. [https://doi.org/10.1175/1520-0426\(2000\)0172.0.CO;2](https://doi.org/10.1175/1520-0426(2000)0172.0.CO;2).

Liu, L., Brangi, V.N., Chandrasekar, V., et al., 1994. Analysis of the copolar correlation coefficient between horizontal and vertical polarizations. *J. Atmos. Ocean. Technol.* 11 (4), 950–960. [https://doi.org/10.1175/1520-0426\(1994\)011<0950:AOTCCC>2.0.CO;2](https://doi.org/10.1175/1520-0426(1994)011<0950:AOTCCC>2.0.CO;2).

- Lund, N.R., Macgorman, D.R., Schuur, T.J., et al., 2009. Relationships between lightning location and polarimetric radar signatures in a small mesoscale convective system. *Mon. Weather Rev.* 137 (12), 4151–4170. <https://doi.org/10.1175/2009MWR2860.1>.
- Ma, Z.J., 1994. *China's Major Natural Disasters and Disaster Reduction Countermeasures* [M]. Science Press, Beijing.
- Mecikalski, R.M., Bain, A.L., Carey, L.D., 2015. Radar and lightning observations of deep moist convection across northern Alabama during DC3: 21 May 2012. *Mon. Weather Rev.* 143 (7), 2774–2794. <https://doi.org/10.1175/MWR-D-14-00250.1>.
- Miller, P.W., Ellis, A.W., Keighton, S.J., 2015. The utility of total lightning trends in diagnosing single-cell thunderstorm severity: examples from the Central Appalachians region. *J. Oper. Meteor.* 3 (8), 82–98.
- Murillo, E.M., Homeyer, C.R., 2019. Severe hail fall and hailstorm detection using remote sensing observations[J]. *J. Appl. Meteorol. Climatol.* 58 (5), 947–970.
- Murphy, M., 2017. Preliminary results from the inclusion of lightning type and polarity in the identification of severe storms[C]. In: 8th Conf. on the Meteor. Appl. of Lightning Data, Seattle, WA, pp. 22–26.
- Murphy, M.J., Said, R.K., 2020. Comparisons of lightning rates and properties from the U.S. National Lightning Detection Network (NLDN) and GLD360 with GOES-16 Geostationary Lightning Mapper and Advanced Baseline Imager data. *J. Geophys. Res.-Atmos.* 125, e2019JD031172.
- Ni, X., Liu, C., Cecil, D.J., et al., 2017. On the detection of hail using satellite passive microwave radiometers and precipitation radar[J]. *J. Appl. Meteorol. Climatol.* 56 (10), 2693–2709.
- Nisi, L., Hering, A., Germann, U., et al., 2020. Hailstorms in the Alpine region: diurnal cycle, 4D-characteristics, and the nowcasting potential of lightning properties[J]. *Q. J. R. Meteorol. Soc.* 146 (733), 4170–4194.
- Ortega, K.L., Krause, J.M., Ryzhkov, A.V., 2016. Polarimetric radar characteristics of melting hail. Part III: Validation of the algorithm for hail size discrimination. *J. Appl. Meteorol. Climatol.* 55, 829–848. <https://doi.org/10.1175/JAMC-D-15-0203.1>.
- Park, H., Ryzhkov, A.V., Zrnica, D.S., et al., 2009. The hydrometeor classification algorithm for the polarimetric WSR-88D: description and application to an MCS. *Weather Forecast.* 24 (3), 730–748. <https://doi.org/10.1175/2008WAF2222205.1>.
- Prein, A.F., Holland, G.J., 2018. Global estimates of damaging hail hazard[J]. *Weather Climate Extrem.* 22, 10–23.
- Ryzhkov, A.V., Kumjian, M.R., Ganson, S.M., et al., 2013a. Polarimetric radar characteristics of melting hail. Part I: Theoretical simulations using spectral microphysical modeling. *J. Appl. Meteorol. Climatol.* 52 (12), 2849–2870. <https://doi.org/10.1175/JAMC-D-13-073.1>.
- Ryzhkov, A.V., Kumjian, M.R., Ganson, S.M., et al., 2013b. Polarimetric radar characteristics of melting hail. Part II: Practical implications. *J. Appl. Meteorol. Climatol.* 52 (12), 2871–2886. <https://doi.org/10.1175/JAMC-D-13-074.1>.
- Schultz, C.J., Petersen, W.A., Carey, L.D., 2009. Preliminary development and evaluation of lightning jump algorithms for the real-time detection of severe weather. *J. Appl. Meteorol. Climatol.* 48, 2543–2563.
- Schultz, C.J., Petersen, W.A., Carey, L.D., 2011. Lightning and severe weather: a comparison between total and cloud-to-ground lightning trends. *Weather Forecast.* 26, 744–755.
- Schuur, T., Ryzhkov, A.V., Heinselman, P., et al., 2003. Observations and classification of echoes with the polarimetric WSR-88D radar. *Natl. Severe Storms Lab. Rep.* 46.
- Scott, R.D., Krehbiel, P.R., Rison, W., 2001. The use of simultaneous horizontal and vertical transmissions for dual-polarization radar meteorological observations. *J. Atmos. Ocean. Technol.* 18 (4), 629–648. [https://doi.org/10.1175/1520-0426\(2001\)018<0629:TUOSHA>2.0.CO;2](https://doi.org/10.1175/1520-0426(2001)018<0629:TUOSHA>2.0.CO;2).
- Sharma, M., Tanamachi, R.L., Bruning, E.C., et al., 2021. Polarimetric and electrical structure of the 19 May 2013 Edmond–Carney, Oklahoma, Tornadic Supercell[J]. *Mon. Weather Rev.* 149 (7), 2049–2078.
- Shi, J., Wang, P., Wang, D., et al., 2019. Radar-based automatic identification and quantification of weak echo regions for hail nowcasting[J]. *Atmosphere* 10 (6), 325.
- Snyder, J.C., Bluestein, H.B., Zhang, G.F., et al., 2010. Attenuation correction and Hydrometeor classification of high-resolution, X-band, dual-polarized mobile radar measurements in severe convective storms. *J. Atmos. Ocean. Technol.* 27 (12), 1979–2001. <https://doi.org/10.1175/2010JTECHA1356.1>.
- Straka, J.M., Zrnica, D.S., Ryzhkov, A.V., 2000. Bulk hydrometeor classification and quantification using polarimetric radar data: synthesis of relations. *J. Appl. Meteorol.* 39, 1341–1372. [https://doi.org/10.1175/1520-0450\(2000\)039<1341:BHCAQU>2.0.CO;2](https://doi.org/10.1175/1520-0450(2000)039<1341:BHCAQU>2.0.CO;2).
- Sun, Y., Xiao, H., Yang, H., et al., 2020. An inverse mapping table method for raindrop size distribution parameters retrieval using X-band dual-polarization radar observations. *IEEE Trans. Geosci. Remote Sens.* 58 (11), 7611–7632. <https://doi.org/10.1109/TGRS.2020.2982687>.
- Tian, Y., Qie, X., Sun, Y., et al., 2019. Total lightning signatures of thunderstorms and lightning jumps in hailfall nowcasting in the Beijing area. *Atmos. Res.* 230, 104646.
- Vivekanandan, J., Zrnica, D.S., Ellis, S.M., et al., 1999. Cloud microphysics retrieval using S-band dual-polarization radar measurements. *Bull. Am. Meteorol. Soc.* 80 (3), 381–388. [https://doi.org/10.1175/1520-0477\(1999\)080<0381:0.CO;2](https://doi.org/10.1175/1520-0477(1999)080<0381:0.CO;2).
- Wang, Y., Chandrasekar, V., 2009. Algorithm for estimation of the specific differential phase. *J. Atmos. Ocean. Technol.* 26, 2565–2578. <https://doi.org/10.1175/2009JTECHA1358.1>.
- Wapler, K., 2017. The life-cycle of hailstorms: lightning, radar reflectivity and rotation characteristics[J]. *Atmos. Res.* 193, 60–72.
- Williams, E.R., Boldi, B., Matlin, A., 1999. The behavior of total lightning activity in severe Florida thunderstorms. *Atmospheric Research* 51, 245–265.
- Wu, F., Cui, X., Zhang, D.L., 2018. A lightning-based nowcast-warning approach for short-duration rainfall events: development and testing over Beijing during the warm seasons of 2006–2007[J]. *Atmos. Res.* 205, 2–17.
- Wu, B., Wei, M., Li, Y., 2022. Dual-polarization radar observations of the evolution of a supercell tornado and analysis of the echo mechanisms[J]. *Atmosphere* 13 (5), 797.
- Zhang, G., Mahale, V.N., Putnam, B.J., et al., 2019. Current status and future challenges of weather radar polarimetry: bridging the gap between radar meteorology/hydrology/engineering and numerical weather prediction. *Adv. Atmos. Sci.* 36, 571–588. <https://doi.org/10.1007/s00376-019-8172-4>.
- Zhao, K., Huang, H., Wang, M., et al., 2019. Recent progress in dual-polarization radar research and applications in China. *Adv. Atmos. Sci.* 36, 961–974.
- Zrnica, D.S., Ryzhkov, A.V., 1999. Polarimetry for weather surveillance radars. *Bull. Am. Meteorol. Soc.* 80 (3), 389–406. [https://doi.org/10.1175/1520-0477\(1999\)080<0389:0.CO;2](https://doi.org/10.1175/1520-0477(1999)080<0389:0.CO;2).
- Zrnica, D.S., Ryzhkov, A.V., Strka, J., et al., 2001. Testing a procedure for automatic classification of hydrometeor types. *J. Atmos. Ocean. Technol.* 18 (6), 892–913. [https://doi.org/10.1175/1520-0426\(2001\)018<0892:0.CO;2](https://doi.org/10.1175/1520-0426(2001)018<0892:0.CO;2).